In situ TEM thermal annealing of high purity Fe10wt%Cr alloy thin foils implanted with Ti and O ions

Martin Owusu-Mensah, Stéphanie Jublot-Leclerc, Aurélie Gentils, Cédric Baumier, Joël Ribis, Vladimir A. Borodin

In situ TEM thermal annealing of high purity Fe10wt%Cr alloy thin foils implanted with Ti and O ions

Martin OWUSU-MENSAH[1], Stéphanie JUBLOT-LECLERC[1], Aurélie GENTILS[1], Cédric BAUMIER[1], Joël RIBIS[2], Vladimir A. BORODIN[3,4]

(1) *CSNSM, Univ Paris-Sud, CNRS/IN2P3, Université Paris-Saclay, Orsay, France*
(2) *DEN, SRMA, CEA, Université Paris-Saclay, Gif sur Yvette, France*
(3) *NRC "Kurchatov Institute", Moscow, Russia*
(4) *National Research Nuclear University MEPhI, Moscow, Russia*

Keywords: Fe-Cr alloy, Titanium, Oxygen, Ion implantation, Thermal annealing, Oxidation, Corrosion, Transmission Electron Microscopy

Abstract

ODS steels are ferritic-martensitic steels reinforced with (Y,Ti) oxide dispersions to enhance the creep and radiation resistance at elevated temperatures. Their conventional fabrication is achieved by ball milling followed by high-temperature consolidation. An alternative approach of ion beam synthesis has been suggested recently to study the early precipitation stages of oxide nanoparticles. To clarify the details of Ti-based oxide nanoparticle precipitation, Ti^+ and O^+ ions were implanted into high-purity Fe-10wt%Cr thin foils at room temperature and subjected to thermal annealing. Nano-size oxide particles and larger surface oxide islands with pronounced Cr enrichment were observed after *in situ* Transmission Electron Microscopy (TEM) annealing at 600°C and were identified as a mixed iron-chromium spinel. The features observed after *ex situ* annealing at 800°C were also identified as iron-chromium oxide, but with a certain titanium enrichment. The observations thus suggest that titanium plays no major role in the early stages of oxide precipitation.

1. Introduction

Ferritic-martensitic (F/M) steels reinforced with a homogeneous distribution of nanosize oxide particles to produce Oxide-Dispersion-Strengthened (ODS) steels are envisaged as excellent candidate structural materials for the fuel cladding in the advanced nuclear Generation IV Sodium Fast Reactors (SFR) and the active zone components of fusion reactors [1-7]. The nanoparticles in these steels serve as obstacles to dislocation motion [8] thereby improving the creep resistance and mechanical properties of steel at elevated temperatures. The standard fabrication of ODS steels employs powder metallurgy method of mechanical alloying. This technique involves mechanical mixing of fine Y_2O_3 and steel powders followed by consolidation at high temperatures using hot isostatic pressing or hot extrusion. Intensive research has been devoted to detailed characterization of resulting nanoparticles, mostly using Transmission Electron Microscopy (TEM) [9-15] and Atomic Probe Tomography (APT) [16-21]. Based on the available data, a number of attempts were undertaken to establish the mechanisms involved in the formation of oxide nanoparticles [15, 22-25], but the suggested mechanisms remain still at best tentative. A more detailed understanding of the mechanisms leading to the nanoparticle precipitation could help to improve and optimize the expensive and time-consuming production process of ODS steels and to further improve their mechanical properties.

To this aim, an alternative approach to synthesize nanoparticles by ion beam synthesis (IBS) has been suggested as a convenient tool for nanoparticle nucleation [26]. The ion beam synthesis technique involves the direct implantation of ions of the desired elements into a solid target followed by post-

implantation heat-treatment in order to force precipitation of nanoparticles and/or nano-layered structures. The ions can be introduced into the target in a controllable way up to desired concentrations, while the implantation parameters such as the temperature and implantation profile can be tuned independently. The IBS approach is straightforward and is widely used in the microelectronics industry, while the mechanisms involved in the implant precipitation are basically understood and could thus help to understand what goes on in the particular case of the metal-oxide precipitation in steels. Our previous studies [27-29] on the successive implantation of Al and O ions into a high-purity FeCr alloy have demonstrated IBS to be a promising tool for clarification of the mechanisms involved in the precipitation of metal-oxide clusters, which in that case were found to be mixed aluminum-chromium oxides. In the present investigation, alternative metal ions, namely those of titanium, were used in attempt to create titanium (or titanium-based) oxide clusters by IBS. For this purpose, Ti and O ions were implanted into thin foils of a high purity Fe-10wt%Cr alloy at room temperature. Subsequent *in* and *ex situ* thermal annealing at temperatures up to 800°C were performed and elemental and crystallographic structure of the observed oxide phases were characterized with Transmission Electron Microscopy based methods. The results obtained are reported in this paper.

2. Experimental Technique

The as-received bulk material was a high-purity FeCr alloy (with 9.86 wt%Cr), obtained from École Nationale Superieure des Mines de Saint-Etienne (France), in the form of a cylindrical piece with the diameter of 1 cm and the length of 1 cm. Smaller pieces of a thickness of approximately 1 mm were cut out of the bulk material. These pieces were then mechanically polished using silicon carbide (SiC) abrasive papers of different grain sizes to obtain the thickness of approximately 100 μm. Circular disks 3 mm in diameter were punched out of these polished pieces, and were subsequently thinned down on both sides and perforated using a twin-jet electro-polisher (Struers Tenupol-5) with a solution of 10% perchloric acid and 90% ethanol at -20°C. The edges of the perforated hole usually had thickness < 100 nm and could be directly inspected by TEM in plane view.

The Ti^+ and O^+ ion implantation experiments were performed on TEM thin foils at the SCALP/JANNUS-Orsay platform located at the Centre de Sciences Nucléaires et de Sciences de la Matière (CSNSM, Orsay, France) [30]. A 190 kV Nier-Bernas source ion implanter IRMA was used for the ion implantations at room temperature. Having in mind the thickness of thin foils (< 100 nm), the projected range of ions was chosen to be at 40-50 nm from the beam-facing surface of the specimen to ensure that the absolute majority of the ions were deposited within the thin foil. The appropriate energies to ensure deposition of ions at this projected range were determined using the Stopping and Range of Ions in Matter (SRIM) code [31] to be 100 and 37 keV for Ti^+ and O^+ ions, respectively. The distribution of ions as a function of depth calculated using the SRIM code is shown in Fig. 1(a). Implantations were performed at room temperature to fluences of 2×10^{16} cm^{-2} and 4×10^{16} cm^{-2} for Ti^+ and O^+ ions, respectively. The ion flux was 7×10^{12} $cm^{-2}s^{-1}$ for both ions. The damage profiles for both ions are also shown in Fig. 1(b). SRIM calculations were performed in Fe using full damage cascades mode using a displacement energy of 40 eV. All the implantations were conducted under vacuum and the samples were positioned perpendicularly to the direction of the ion beam. No significant heating of the samples was expected for these implantation conditions at room temperature.

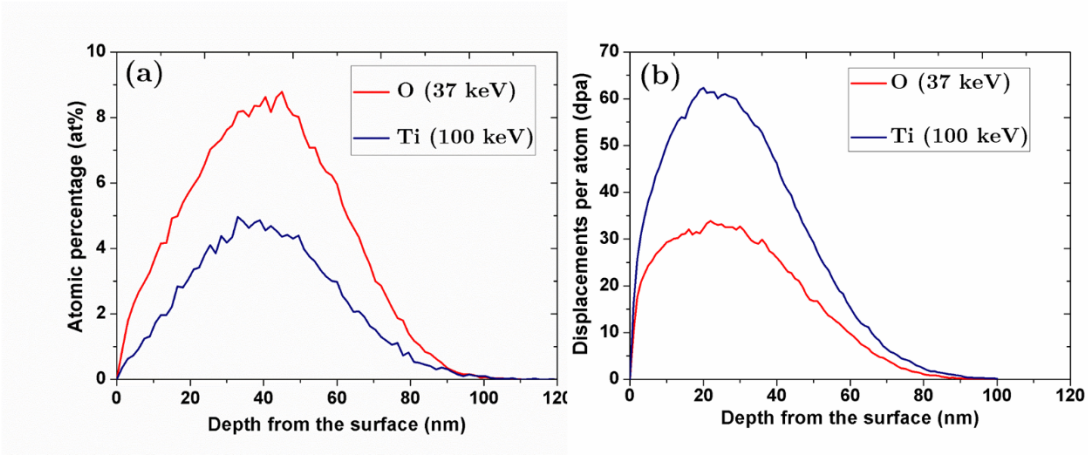

Figure 1. (a) Concentration profiles and (b) damage profiles of implanted O^+ and Ti^+ ions as a function of the depth from the thin foil surface at the fluences of $4x10^{16}$ cm^{-2} for O^+ and $2x10^{16}$ cm^{-2} for Ti^+, calculated using SRIM software in Fe in full damage cascades mode using a displacement energy of 40 eV.

Post implantation high-temperature annealing was carried out on thin foils after TEM observation of the as-implanted sample structure. The annealing of implanted thin foils was performed *in situ* in the vacuum column of Tecnai G^2 20 twin TEM at the SCALP/JANNuS-Orsay facility, using a high-temperature Gatan sample holder, which allows heating up to 800°C. The sample holder was connected to a temperature monitor and a water tube for temperature regulation during the experiment and subsequent cooling. The vacuum pressure during the annealing runs was approximately 1.2×10^{-5} Pa. The *in-situ* annealing runs were undertaken at 500°C and then at 600°C. Annealing temperatures were reached in approximately 15 minutes and the annealing runs themselves were performed for 90 minutes. Already at 600°C, the indications of iron loss from the FeCr matrix into the vacuum chamber were noticed. Hence, in order to avoid the vacuum chamber contamination, the annealing of thin foils at the even higher temperature of 800°C was done *ex situ* for 2 hours in a vacuum chamber with a pressure similar to that within TEM.

Characterization of the samples was performed both during and after annealing experiments. Conventional TEM techniques, namely, the bright field (BF) and dark field (DF) imaging, as well as diffraction pattern (DP) analysis were used to check for the presence of new phase precipitates. The chemical composition and crystallographic structure of the found precipitates were investigated with analytical TEM techniques using two different microscopes. The first one was a 200 kV FEI Tecnai G^2 20 Twin microscope located at CSNSM/JANNuS-Orsay and equipped with a Gatan Imaging Filter (GIF) and an Energy Dispersive X-ray (EDX) spectrometer. The microscope was used for all the *in situ* conventional TEM imaging as well as the EDX and Energy-Filtered TEM (EFTEM) investigations. EDX analysis was also performed on as-received samples to confirm the near to zero presence of any impurities and ~10%Cr content in the FeCr alloy, as well as on the implanted specimens to verify the Ti and O presence after annealing. Energy filtered TEM elemental maps were acquired for the base alloy constituents, Fe and Cr, and for the implanted elements, Ti and O, at different stages of the experiment. The elemental maps were taken from the core loss region using both the jump ratio method and the three-window method. The relevant edge energy thresholds for Fe, Cr, Ti and O were Fe-$L_{2,3}$ at 708 eV, Cr-$L_{2,3}$ at 575 eV, Ti-$L_{2,3}$ at 432 eV and O-K at 532 eV. The original images have the grayscale contrast (dark and bright images). An additional colour coding was superimposed on the grayscale elemental maps in order to make the maps easily identifiable. The second microscope employed in this study was a JEOL 2010F FEG TEM operating at 200 kV located at SRMA (CEA Saclay, University of Paris-Saclay, France); it was used for post-annealing HRTEM imaging.

3. Results and discussion

3.1. As-implanted Samples

The Ti and O ion implantations at room temperature have produced no particles visible in TEM thin foils when observed in bright field (BF) imaging conditions. The diffraction patterns of the samples show no reflections in addition to those of the Fe-Cr matrix, while EFTEM analytical characterization shows homogeneous (spatially uniform) elemental distributions.

3.2. Post implantation *in situ* annealing at 500 and 600°C

After the *in situ* annealing at 500°C, the presence of precipitated particles was not evident on BF images due to the high density of dislocations/defects created by the ion implantation, which led to a weak imaging contrast. However, additional spots appeared on diffraction patterns, which, when used to produce dark-field (DF) images, revealed nanometer-size white dots that were too small for identification. Hence, the samples were additionally annealed *in situ* at 600°C in order to force these dots coarsen for easier characterization. During the course of the annealing, one could notice the formation of areas with white contrast at the periphery of the hole (see Fig. 2) where the specimen was very thin. These white regions were growing with time to cover thicker regions, whilst smaller white regions were gradually appearing away from the hole, as can be seen in Fig. 2(a).

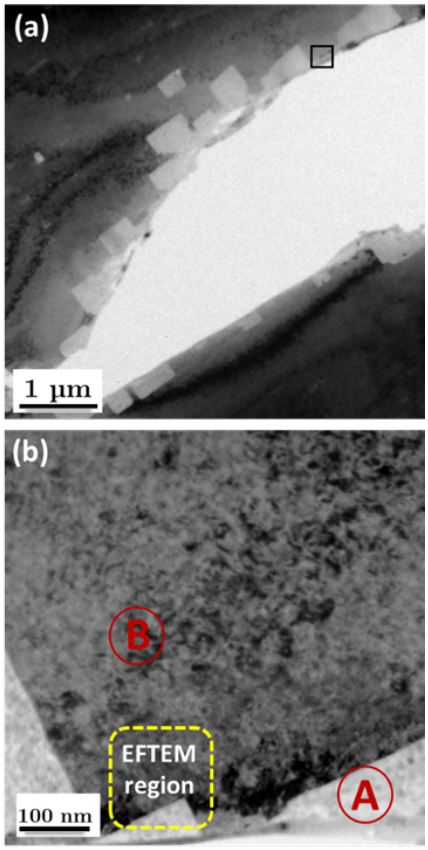

Fig 2. (a) BF image of the thin foil after annealing at 600°C with distinct white contrast islands observed close to the hole. (b) Magnified image of the zone outlined in panel (a), which shows two regions, namely region [A] closest to the hole and region [B] farther away from the hole, as well as the region chosen for EFTEM analysis (surrounded with the dashed line).

EFTEM elemental maps were acquired on different regions of the annealed thin foil. The results obtained in the region highlighted in Fig. 2, including both the white contrast region close to the hole (A) and the region with small white dots (B), are reported in Fig. 3. The BF image and EFTEM elemental maps were acquired with a large objective aperture responsible for low contrast in the BF image. On

the EFTEM elemental maps, regions with darker contrasts represent deficiency or depletion of an element, whilst the brighter (colored) contrasts correspond to its enrichment. Clearly, region B contains small areas with elemental contrast matching that of region A. Both these small areas and region A are enriched in chromium and oxygen and depleted in iron. The depletion in iron only implies its lower concentration compared to the matrix; the presence of iron cannot be excluded in these areas. The titanium elemental map appears uniform in region B. The slightly brighter contrast of the Ti map in region A is due to the variation in thickness. The uniform Ti distribution was observed in multiple other Ti maps acquired all over the specimen.

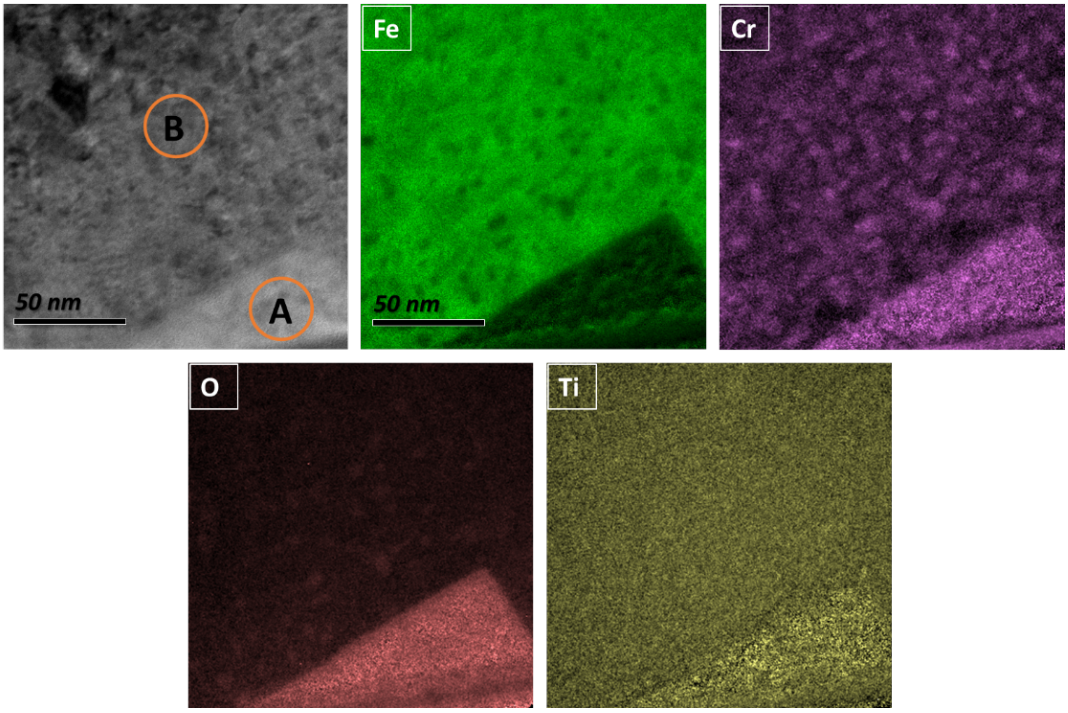

Figure 3. Bright Field (BF) image of the chosen region together with EFTEM elemental maps acquired using the jump-ratio method in the vicinity of Fe-$L_{2,3}$ edge, Cr-$L_{2,3}$ and Ti-$L_{2,3}$ edges for the thin foil implanted at room temperature and annealed at 600°C for 90 minutes.

Diffraction patterns acquired both for the white-contrast region A and for region B apart from it are given in Figs. 4(a) and (b), respectively. In the diffraction pattern in Fig. 4(a), both single crystal diffraction spots and polycrystalline rings are observed. The single crystal diffraction in Fig. 4(a) corresponds to *fcc*-like crystal structure in the zone axis B = $[\bar{1}12]$. From the measured inter-planar spacings and angles, the lattice parameter is determined to be 0.84 nm. The definite chromium enrichment in the white contrast areas suggests that they correspond to some form of a mixed iron-chromium oxide $Fe_{3-x}Cr_xO_4$ with spinel structure, which has very similar lattice parameter (a = 0.845 nm [32]) for the wide range of chromium content variation from pure iron oxide Fe_3O_4 (magnetite) up to chromite $FeCr_2O_4$. In Fig. 4(b), the single crystal diffraction spots connected with the orange line appear to correspond to some cubic (*bcc* or *fcc)* crystal structure with the orientation B = [001]. The measured interplanar spacing matches that of the *bcc* Fe-Cr matrix. In addition, one observes the set of spots shown interconnected with green lines in Fig. 4(b). The measured interplanar spacings and angles match those of mixed iron-chromium spinel oriented along B= [-114]. The similarity of both the diffraction and the elemental contrasts on region A and on the small areas in region B indicates that a similar compound is formed in these regions.

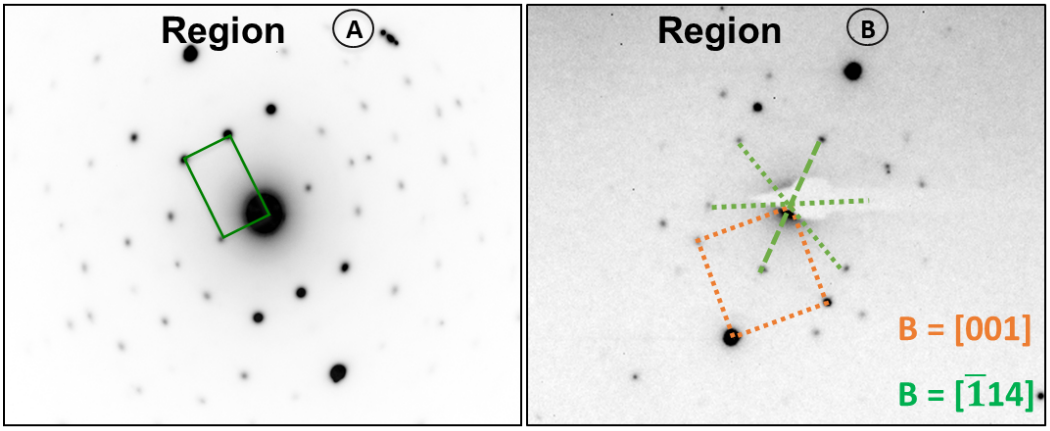

Fig. 4. Diffraction patterns corresponding to (a) region A with white contrast as observed in Fig. 3 and (b) the thicker region B farther away from the hole.

The diffraction results for the composition of the precipitated phase are supported by EELS quantification performed in a large white region similar to region A, which has demonstrated twice as much chromium (~ 15%) as iron (~ 9%) and a high amount of oxygen (~ 74%), indicating the layer composition close to that of chromite, $FeCr_2O_4$. In a region similar to region B, away from the hole, the ratio of Fe and Cr concentrations was close to the expected ratio of 1:10 in the FeCr matrix and the O amount was much less important. The amount of Ti was found to be similar in both regions, confirming the absence of Ti enrichment in the white region A.

The early formation of iron-chromium oxide in the very thin edges of the specimen, its dominance close to the hole and its expansion with time and temperature of annealing towards thicker regions indicate that it predominantly forms surface islands on the thin foil. The thinnest regions of white contrast at the hole edge, similar to region A, are made basically of oxide, whilst the thicker regions seem to be the matrix covered with Cr-enriched oxide scales.

It is reasonable to expect that the large surface oxide islands form as a result of the Fe-Cr alloy oxidation by oxygen and other gases (CO_2, moisture) remaining in the vacuum chamber after pumping out. The contribution of oxidation after the electro-polishing stage in the sample preparation cannot be discounted. The nature of very small spots observed farther from the sample edge is less clear. These can be oxide precipitates formed inside the bulk from the implanted oxygen ions, but they can be as well nuclei of surface oxide formed due to the reaction with the residual oxygen from the vacuum. Whatever the case, they contain no traces of titanium.

The formation of surface oxide layer with the obvious chromium enrichment is rather unexpected. More typical for iron-chromium alloys with our level of Cr content is the observation of duplex oxide layers, independent of the corrosive environment [33-38]. Such duplex scales consist of the outer magnetite layer and internal layer of mixed iron-chromium oxide (with the chemical composition close to Fe_2CrO_4 [38], rather than $FeCr_2O_4$). However, it is usually assumed that iron and chromium only redistribute over the oxide layer depth, so no net iron depletion or in chromium enrichment is expected in EFTEM maps when looking in plane view.

The observed enrichment of oxide layer in chromium, which is especially pronounced at the completely oxidized hole edges, where the local Cr to Fe ratio changes to ~2:1 from 1:9 in the bulk, can be only explained if one assumes that the large share of iron is lost in the vacuum during oxidation. The loss of iron readily explains the white contrast in region A in Fig. 2 and in similar other regions close to the hole that have been thinned by the oxidation process. The observed loss of iron is not necessarily contradictory to the standard picture of the duplex oxide formation, because the latter is commonly recorded when the oxide scale thickness is already microns and more, while in our case it is at best

several tens of nanometers. However, it gives indications that the duplex oxide formation might start only after a certain delay, while at the very early oxidation stages the oxidation kinetics is governed by the direct penetration of oxygen into the iron-chromium matrix, while some iron is lost in the environment.

The loss of iron atoms is highly undesirable in *in situ* TEM experiments because of the vacuum contamination and potential iron deposition on the pole pieces. For this reason, it was decided to perform the annealing at higher temperatures in *ex situ* regime, rather than in *in situ* one.

3.3. Post implantation annealing at 800°C

Similar to the lower-temperature *in situ* annealing, one could observe the extensive growth of surface oxide, including both large islands close to the hole and nanometre size regions (with the average diameter of ≈9 nm) farther from it. HRTEM imaging was performed on different areas in several regions of the implanted thin foils annealed at 800°C. Fig. 5(a) shows a HRTEM image of a selected region of the sample showing a particle with the diameter of approximately 12 nm surrounded by the matrix. The Fast Fourier Transform (FFT) analysis of selected areas inside the matrix and inside the particle are shown in Figs. 5(b) and (c), respectively. In Fig. 5(b) one observes the common diffraction pattern of Fe-Cr matrix with the zone axis B = [111]. For the particle, different structures can result in the observed FFT pattern. It could correspond to a *bcc-type* structure in the zone axis B= [111], but equally well to *fcc-type* structure with B = [111] or hexagonal closed packed (*hcp)* structure with B = [0001]. However, the interplanar distances for these potential structures in corresponding zone axes only matched those of iron-chromium spinel among a variety of different possible oxide compounds (including also Fe_2O_3, Cr_2O_3, TiO, TiO_2- anatase, brookite, rutile, Ti_2O_3) that we have checked, assuming B = [111] zone axis. Similar results were obtained both for large surface oxide islands and smaller regions.

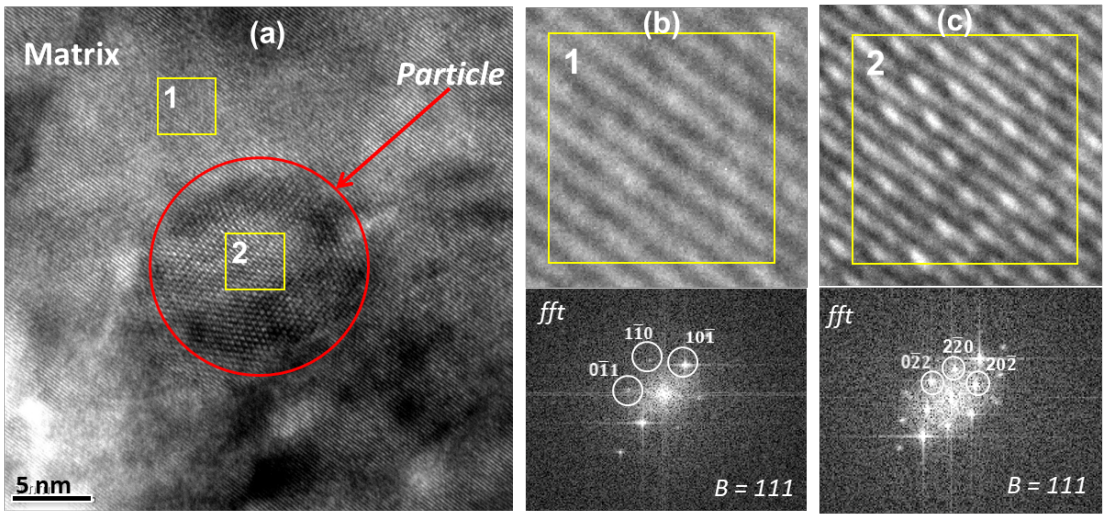

Fig. 5. (a) HRTEM image of a particle in the matrix, with the squares denoting regions used for analysis. (b) Magnified image of the atomic planes in square 1 (bottom) and its calculated FFT for the FeCr matrix, (c) Same as (b), but for the particle (square 2).

EFTEM elemental maps, such as those reported in Fig. 6, indicate that both large and smaller features are depleted in Fe and enriched in Cr and O. In addition, in contrast to lower temperature annealing, one can notice that these zones are clearly enriched in Ti, see Fig. 6(d).

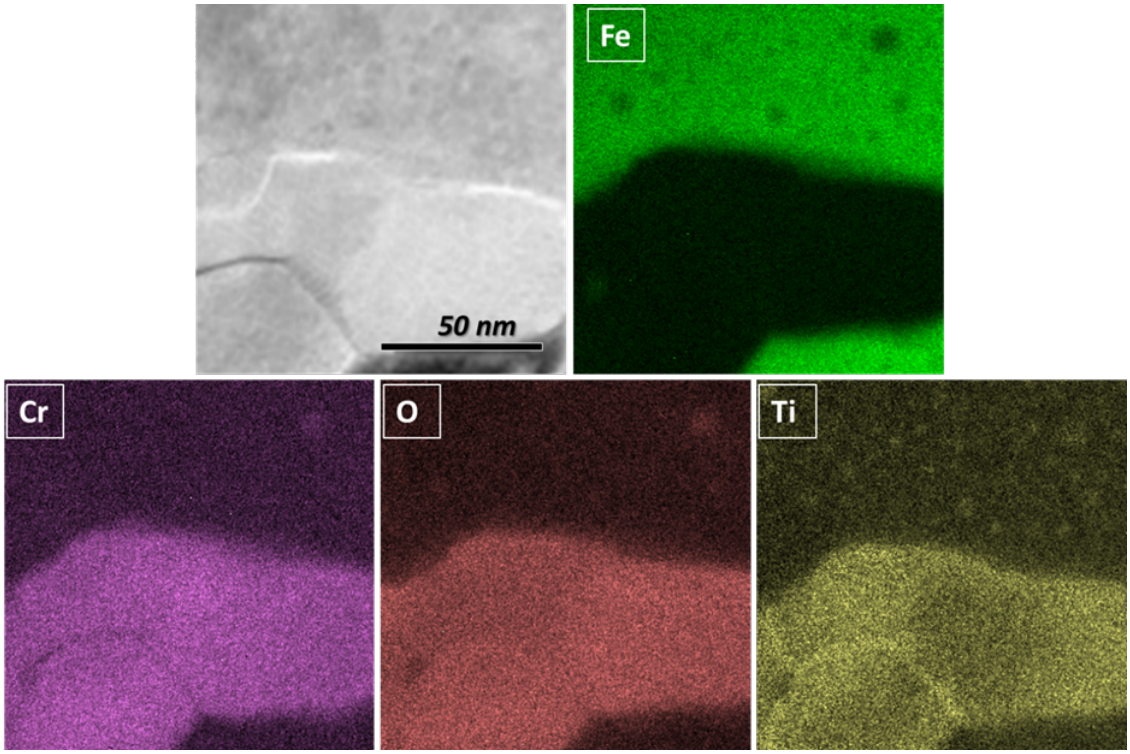

Figure 6. Energy-Filtered TEM (EFTEM) elemental characterization of the thin foil implanted at room temperature and annealed at 800°C for 2 hours. Bright Field (BF) image of the region chosen for EFTEM together with elemental maps acquired using the two-window jump ratio method in the vicinity of Fe-$L_{2,3}$ edge, Cr-$L_{2,3}$, O-K and Ti-$L_{2,3}$ core loss edges.

To confirm the Ti enrichment in oxide areas, a STEM-EDX investigation was carried out on one of the large islands. Figure 7 shows a particle with the size of approximately 100 nm, which is surrounded by a white contrast region. EDX spectral imaging was conducted running through the particle as indicated in Fig. 7(a). Four distinct zones are highlighted. Both zones 1 and 4 are located in the matrix outside the particle, zone 2 resides within the particle and zone 3 represents the white contrast region around the particle. The corresponding measured spectra are reported in Fig. 7(c). The spectra in zones 1 and 4 show a very intense peak for iron, a weaker peak for chromium and a much weaker peak for titanium, as expected for Fe-Cr matrix. The O-K peak overlaps with the Cr-L peak at low energy (roughly 0.5 eV), and hence, an accurate quantification cannot be achieved. In zones 2 and 3, the Cr, Ti and O peaks are significantly more intense than in the matrix (zones 1 and 4) while the Fe peak is noticeably weaker. The relative intensity of peaks in zones 2 and 3 are roughly equivalent but, compared to all other spectra, the spectrum of zone 3 with the white contrast has much less counts, which suggests that zone 3 is a very thin region. As in Fig. 2, the white contrast mainly results from the thinning of zone 3 due to the loss of iron. The STEM-EDX results are in agreement with the assumption that the observed particles are (Fe,Cr) oxides that are to a certain degree enriched in Ti, as suggested by EFTEM.

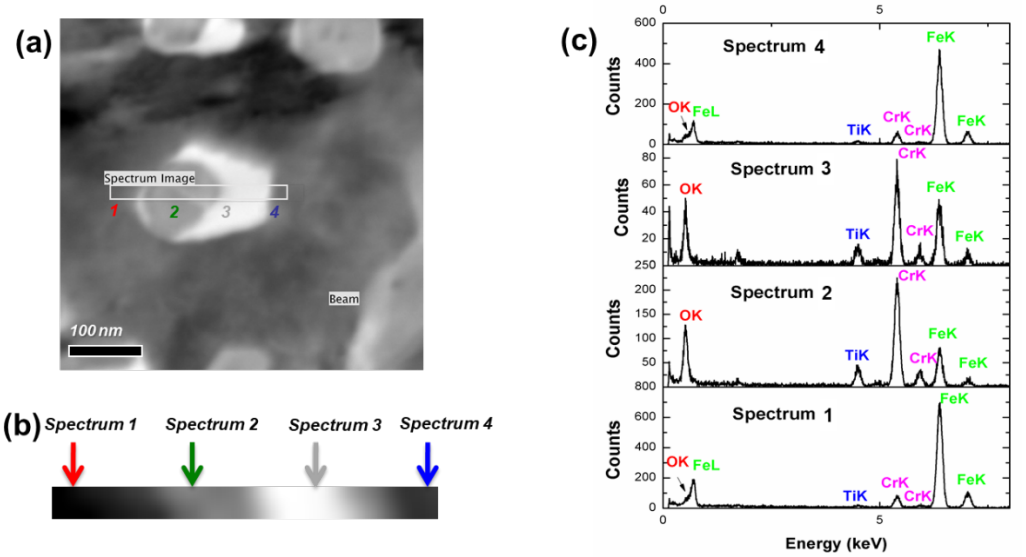

Figure 7. (a) BF image of a particle. The area on which line spectrum imaging was performed is marked with a rectangle and the numbers indicate four different regions used for the analysis. (b) Line spectrum-imaging with the pixels from which EDX spectra are extracted; (c) STEM EDX spectra for the chosen regions, as indicated in panel (a).

Conclusions

1. Implantation of Ti^+ and O^+ ions into high purity Fe-Cr thin foils has been performed at room temperature. No visible nano-particles appear to have precipitated during implantation.

2. Small particles with the diameter of the order of 5 nm as well as large islands of approximately 200 nm size were formed close to the hole in the thin foil after *in situ* TEM annealing at 500 and 600°C. The composition and structure of these particles are compatible with those of mixed iron-chromium spinel typically formed on the surface of steels with similar Cr content as a result of corrosion. The islands formed at the thin edges of the hole grew in time to cover thicker regions indicating that this iron-chromium oxide predominantly forms at the surface of the foil. The smaller oxide spot location (either on the surface, or in the bulk) could not be unambiguously identified. However, in either case no identifiable precipitation of Ti could be identified.

3. Enhanced annealing at 800°C resulted in a qualitatively similar picture, with the only exception that the observed iron-chromium oxides were additionally somewhat enriched in Ti. This indicates that implanted titanium begins to participate in the oxide precipitation in the temperature range somewhere between 600 and 800°C, but even at 800°C its role in the oxide formation remains rather marginal. It can be expected, however, that annealing at higher temperatures might promote more active titanium participation in oxide formation.

4. The observation of iron depletion and chromium enrichment in the surface oxide islands (up to complete conversion into chromite in the fully oxidized film areas close to the hole) does not fall into the common picture of duplex oxide layer formation during environmental corrosion of steels with similar Cr content. This may be indicative of the fact that at the very early oxidation stages, when the oxide thickness is within tens of nanometers, a noticeable share of iron is lost in the environment, rather than promotes the outer magnetite layer formation. The nature of the environment (vacuum, air, water etc.) might also play a role.

5. The formation of a mixed iron-chromium spinel on the surfaces of the Fe-Cr thin foil could hinder the observation and possibly formation of small nanoparticles beneath the surface. This phenomenon of corrosion could in principle occur in any *in situ* experiment performed on steels at elevated temperature. This is a major drawback that has to be taken into account depending on the nature of the experiment,

and if possible minimised by limiting the duration and/or temperature of annealing and better controlling the amount of oxygen on the surfaces of the thin foil and in the column of the TEM. For the present study, from the methodological point of view, the strong surface oxidation in the standard vacuum of TEM vacuum chamber demands the improvements in the microstructure characterization approach. In particular, observations in cross-section will be instructive to establish what happens beneath the surface of the ion implanted and annealed samples [39].

Acknowledgements

The authors thank Lucie Delauche for the assistance in sample preparation. The authors acknowledge the efforts of the SCALP/JANNuS-Orsay technical staff for the ion implantations, especially Stéphane Renouf and Jérôme Bourçois. Martin Owusu-Mensah acknowledges PHENIICS doctoral school of Université Paris-Sud/ Universite Paris-Saclay for the funding of his PhD thesis. This work has been carried out within the framework of the EUROfusion Consortium and French Research Federation for Fusion Studies and has received funding from the Euratom research and training programme 2014–2018 under grant agreement No. 633053. The views and opinions expressed herein do not necessarily reflect those of the European Commission.

References

[1] S. Ukai, H. Okada, M. Inoue, T. Nishida, M. Fujiwara, S. Nomura, S. Shikakura, and K. Asabe, J. Nucl. Mater. 204 (1993) 65.

[2] S. Ukai and M. Fujiwara, J. Nucl. Mater. 307 (2002) 749.

[3] P. Yvon and F. Carré, J. Nucl. Mater. 385 (2009) 217.

[4] J. Sik, C. Bock, B. Oon, J. P. Raison, T. Mizuno, F. Delage, and J. Carmack, J. Nucl. Mater. 392 (2009) 324.

[5] S. J. Zinkle, Fusion Engineering and Design, 74, (2005) 31.

[6] Y. De Carlan, J. Bechade, P. Dubuisson, J. Seran, P. Billot, A. Bougault, T. Cozzika, S. Doriot, D. Hamon, J. Henry, M. Ratti, N. Lochet, D. Nunes, P. Olier, T. Leblond, and M. H. Mathon, J. Nucl. Mater. 386 (2009) 430.

[7] A. F. Tavassoli, E. Diegele, R. Lindau, N. Luzginova, and H. Tanigawa, J. Nucl. Mater. 455 (2014), 269.

[8] S. J. Zinkle and J. T. Busby, Mater. Today 12 (2009) 12.

[9] M. Klimiankou and R. Lindau, J. Nucl. Mater. 333, (2004), 347.

[10] M. Klimenkov, R. Lindau, and A. Möslang, J. Nucl. Mater. 386 (2009) 553.

[11] Y. Wu, E. M. Haney, N. J. Cunningham, and G. R. Odette, Acta Materialia, 60 (2012), 3456.

[12] J. Ribis and Y. de Carlan, Acta Mater. 60 (2012) 238.

[13] M. Loyer-Prost, J.-S. Merot, J. Ribis, Y. Le Bouar, L. Chaffron, F. Legendre, J. Nucl. Mater. 479 (2016) 76.

[14] P. Dou, A. Kimura, R. Kasada, T.Okuda, M. Inoue, S. Ukai, S. Ohnuki, T. Fujisawa, F. Abe, S. Jiang, and Z. Yang, J. Nucl. Mater. 485 (2017) 189.

[15] X. Zhou, Z. Ma, L. Yu, Y. Huang, H. Li Y. Liu, J. Mater. Sci. 54 (2019) 7893.

[16] M. K. Miller, K. F. Russell, and D. T. Hoelzer, J. Nucl. Mater. 351 (2006), 261.

[17] E. A. Marquis, Applied Physics Letters. 181904 (2008) 1.

[18] C. A. Williams, E. A. Marquis, A. Cerezo, and G. D. W. Smith, J. Nucl. Mater. 400 (2010) 37.

[19] A.A. Aleev, N.A. Iskandarov, M. Klimenkov, R. Lindau, A. Möslang, A.A. Nikitin, S.V. Rogozhkin, P. Vladimirov, A.G. Zaluzhnyi, J. Nucl.Mater. 409 (2011) 65.

[20] S.V. Rogozhkin, A.A. Aleev, A.G. Zaluzhnyi, A.A. Nikitin, N.A. Iskandarov, P. Vladimirov, R. Lindau, and A. Möslang, J. Nucl.Mater. 409 (2011) 94.

[21] K.D. Zilnyk, K.G. Pradeep, P. Choi, H.R.Z. Sandim, D. Raabe, J. Nucl.Mater. 492 (2017) 142.

[22] C. Hin, B. D. Wirth, and J. B. Neaton, Phys. Rev. B. 80 (2009) 134118.

[23] C. Hin and B. D. Wirth, Mater. Sci. Eng. A, 528 (2011) 2056.

[24] C. L. Fu, M. Krcmar , G. S. Painter, X. Chen, Phys. Rev. Lett. 99 (2008) 225502.

[25] Y. Jiang, J. R. Smith, and G. R. Odette, Phys. Rev. B. 79 (2009) 064103.

[26] D. Sakuma, S. Yamashita, K. Oka, S. Ohnuki, L. E. Rehn, and E. Wakai, J. Nucl. Mater. 329, 392 (2004).

[27] C. Zheng, A. Gentils, J. Ribis, O. Kaïtasov, V. A. Borodin, M. Descoins, and D. Mangelinck, Philos. Mag. 94 (2014) 2937.

[28] C. Zheng, A. Gentils, J. Ribis, V. A. Borodin, O. Kaïtasov, and F. Garrido, Nucl. Inst. Methods Phys. Res. B, 365 (2015) 319.

[29] C. Zheng, A. Gentils, J. Ribis, V. A. Borodin, M. Descoins, D. Mangelinck, F. Dalle, B. Arnal, L. Delauche, C. Zheng, A. Gentils, J. Ribis, V. A. Borodin, M. Descoins, and D. Mangelinck, J. App. Phys. 121 (2017) 174305.

[30] CSNSM, Available: https://www.csnsm.in2p3.fr/. [Accessed: 23-Jan-2019].

[31] James F. Ziegler, J. P. Biersack, U. Littmark, The Stopping and Range of Ions in Solids (Pergamon Press, New York, 1996).

[32] P. Villars and L. D. Calvert, Pearson's Handbook of Crystallographic Data for Intermetallic Phases - Volume 2, Second Edi. Ohio: American Society for Metals, 1986.

[33] L. Martinelli, F. Balbaud-célérier, A. Terlain, S. Delpech, G. Santarini, and J. Favergeon, Corrosion Science, 50 (2008) 2523.

[34] L. Martinelli, F. Balbaud-célérier, G. Picard, and G. Santarini, Corros. Sci. 50 (2008) 2549.

[35] J. Isselin, R. Kasada, and A. Kimura, Corros. Sci. 52 (2010) 3266.

[36] J. Bischoff and A. T. Motta, J. Nucl. Mater. 430 (2012) 171.

[37] F. Rouillard G. Moine L. Martinelli, and J. C. Ruiz, Corros. Sci. 77 (2012) 27.

[38] L. Martinelli, C. Desgranges, F. Rouillard, K. Ginestar, M. Tabarant, and K. Rousseau, Corros. Sci. 100 (2015) 253.

[39] Martin Owusu-Mensah, Aurélie Gentils, Stéphanie Jublot-Leclerc, Joël Ribis, Ryan Schoell, Djamel Kaoumi, Vladimir A. Borodin, submitted to Acta Materialia.